

# *In Situ* Monitoring of the Growth, Intermediate Phase Transformations and Templating of Single Crystal VO<sub>2</sub> Nanowires and Nanoplatelets

Evgheni Strelcov,<sup>†</sup> Albert V. Davydov,<sup>‡</sup> Uday Lanke,<sup>§</sup> Clay Watts,<sup>†</sup> and Andrei Kolmakov<sup>†,\*</sup>

<sup>†</sup>Department of Physics, Southern Illinois University at Carbondale, Illinois 62901-4401, United States, <sup>‡</sup>Metallurgy Division, MML, NIST, Gaithersburg, Maryland 20899, United States, and <sup>§</sup>Canadian Light Source Inc., Saskatoon, SK S7N 0 × 4, Canada

VO<sub>2</sub> single-crystalline quasi-1D nanostructures recently received significant attention due to their uniquely sharp onset of the temperature driven metal–insulator transition (MIT) and the intimate coupling of the MIT with mechanical, optical, thermal, and electronic properties of these nanostructures.<sup>1–5</sup> This coupling can be used in ultrafast optical switchers, electronic and gas-sensing devices,<sup>6</sup> and electromechanical actuators.<sup>7</sup> Similar to other semiconductor nanowires,<sup>8</sup> the use of VO<sub>2</sub> nanowires (NWs) in these and other applications requires precise control over their structure, spatial position, orientation, and surface density. A variety of protocols for VO<sub>2</sub> NW high-temperature synthesis has been published in recent years.<sup>1,3,4,9,10</sup> In most of these reports, physical vapor transport and condensation of VO<sub>2</sub> precursors on the preferable facets of the VO<sub>2</sub> nuclei at ~1000 °C were presumed to be the major steps of VO<sub>2</sub> nanowire growth.<sup>1,2</sup> It was soon realized that pure vanadium dioxide is too refractory ( $T_m = 1542\text{ °C}^{11}$ ) to be responsible for appreciable vapor mass transfer to the substrate,<sup>10,12</sup> especially since VO<sub>2</sub> nanostructures have been obtained at much lower temperatures (e.g., at 550–650 °C<sup>10</sup>). To explain this phenomenon and the presence of liquid phases of vanadium oxides at the intermediate stages of NW growth, the involvement of low-melting V<sub>2</sub>O<sub>5</sub> ( $T_m \approx 690\text{ °C}$ ) was invoked. Following *ex situ* SEM studies, evidence of participation of V<sub>2</sub>O<sub>5</sub> liquid microdroplets in VO<sub>2</sub> NW growth has been recently reported.<sup>10,12</sup>

Traditional after-growth analysis of the resultant VO<sub>2</sub> nanostructures by means of SEM, HRTEM, SPM, and associated spectroscopies has led to significant understanding

**ABSTRACT** Direct *in situ* optical and photoelectron emission microscopy observations of the nucleation and growth of VO<sub>2</sub> meso- and nanostructures using thermal transport of V<sub>2</sub>O<sub>5</sub> precursor in a vacuum or in an inert-gas environment were conducted. During nanostructure reductive growth, the formation, coexistence, and transformation of the intermediate oxide phases and morphologies were observed and characterized structurally and compositionally. The composition, structure, and morphology of the resultant nanostructures appeared to be a product of the interplay between kinetic and thermodynamic factors during multiple phase transformations. By rationally “navigating” the growth parameters using knowledge of the vanadium–oxygen temperature–composition phase diagram, wetting behavior, and epitaxial relationships of the intermediate phases with the substrate, control over growth direction, faceting, shape, and elastic strain of the nanostructures can be achieved. Such versatile control over the properties of single-crystal VO<sub>2</sub> nano- and mesostructures will facilitate their application in MEMS, sensors, and optoelectronics.

of VO<sub>2</sub> nanostructure formation. However, recent grazing incidence small-angle X-ray scattering (GISAXS) experiments<sup>10</sup> on real-time monitoring of VO<sub>2</sub> nanostructure growth demonstrated the great potential of *in situ* analysis techniques of growth processes at the meso- and nanoscale.

In spite of the demonstrated usefulness of such *in situ* SEM, TEM, SPM, and X-ray diffraction techniques,<sup>13–17</sup> their application at elevated temperatures and in a controlled gas environment remains an experimental challenge. On the other hand, the development of optics and imaging protocols in traditional optical microscopy now make it possible to routinely image isolated objects as small as 40 nm across (i.e., Ag nanoparticles) and as thin as single graphene sheets, well below the diffraction limit of visible light.<sup>18</sup> Hot stages for optical microscopes have been used to study crystal growth for more than a century,<sup>19,20</sup> but their application in studying nanowire and whisker growth has been largely overlooked.

\* Address correspondence to akolmakov@physics.siu.edu.

Received for review February 21, 2011 and accepted March 23, 2011.

Published online March 23, 2011  
10.1021/nn2007089

© 2011 American Chemical Society

As presented in this paper, using a custom-made planar hot stage coupled with a high-quality optical microscope we were able to monitor the nucleation and growth of vanadium dioxide nano- and mesostructures *in situ*, in real time, and in a wide temperature range. The direct real-time visualization of these processes allowed us to revisit and refine previous VO<sub>2</sub> growth models and propose protocols for the rational fabrication of nanostructures.

## RESULTS AND DISCUSSION

**Typical Morphologies of As-Grown VO<sub>2</sub> Nano- and Mesostructures.** The SEM images in Figure 1a were collected from different areas of the same sample and represent typically obtained morphologies of VO<sub>2</sub> nano- and mesostructures grown on a Si substrate with a native oxide layer as a function of the deposition rate. As can be seen (left panel, Figure 1a), a low flux of the precursor results in thin, short VO<sub>2</sub> nanowires with a typical diameter of 100–200 nm, while substrate areas exposed to higher precursor flux demonstrate gradual increase in the diameter and the length of the nanowires (Figure 1 a, left to right). With increase of the precursor deposition rate, the thickness of the nanostructures stabilizes in the 10<sup>2</sup> to 10<sup>3</sup> nm range, and the deposit adopts the morphology of separate, irregular platelets of a few micrometers wide. At even higher fluxes, the preferential uniaxial growth halts and individual single-crystal quasi-2D platelets merge to form a complete polycrystalline film. The irregular

and smooth (on a large scale) shape of the borders of the individual platelets as opposed to the well-faceted shape of NWs suggests stabilization of the higher energy facets at the intermediate stages of growth. The morphology of these platelets depends on the substrate and on the thickness of the SiO<sub>2</sub> layer in particular (see Discussion section below). Figure 1b shows a typical microbelt formed on Si wafers with a thick (>100 nm) thermally grown SiO<sub>2</sub> layer. The existence of characteristic ferroelastic domains seen in polarized reflected light (Figure 1b,c) is a manifestation of the elastic strain induced in the platelets due to the difference in thermal expansion coefficients of the strongly adhered VO<sub>2</sub> and the substrate.<sup>21,22</sup> As a result, the size and orientation of domains are related to the substrate induced strain, which rises with increasing SiO<sub>2</sub> thickness (compare Figure 1 panels b and c). The thermally driven MIT in films made of such percolating platelets is significantly broader than that in individual nanostructures or platelets and is due to incoherency of the metal phase nucleation in different platelets (grains).

To elucidate in depth the particularities of the VO<sub>2</sub> NW growth mechanism, we conducted detailed studies inside a hot stage (see Methods section) custom designed for *in situ* optical microscopy monitoring of surface morphology as a function of temperature and gaseous environment. The precursor was delivered to the substrate in two different ways. In direct deposition (DD) mode, the precursor (a fine powder of V<sub>2</sub>O<sub>5</sub>) was

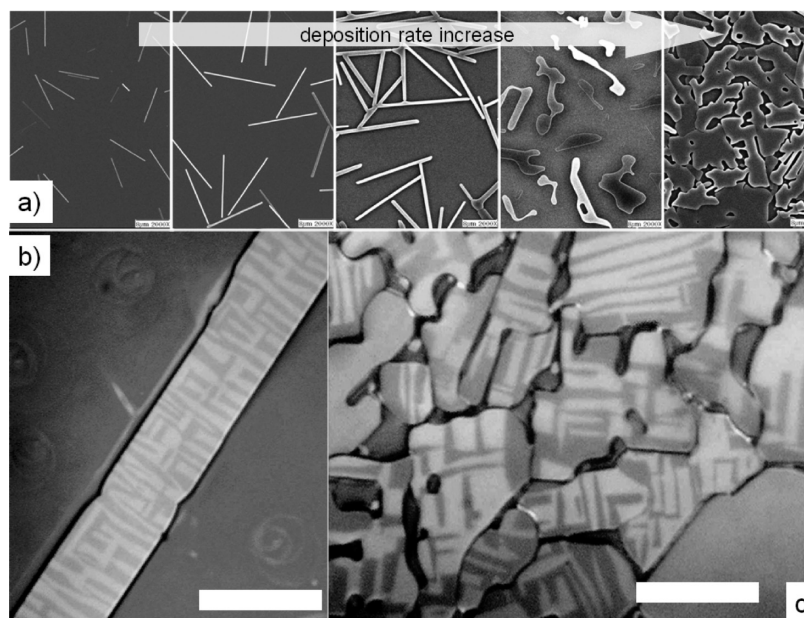
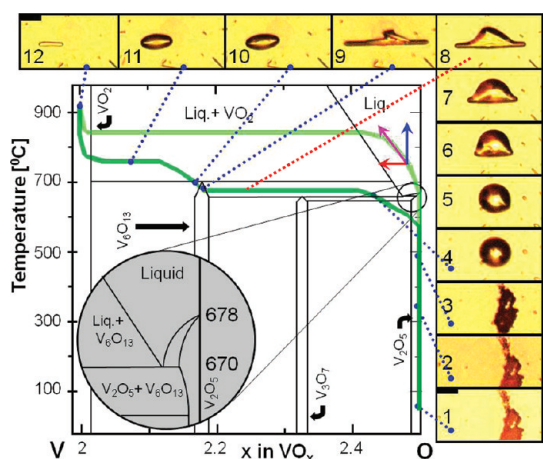


Figure 1. (a) SEM images of the VO<sub>2</sub> nanostructures grown inside a tube furnace on a Si wafer (with native SiO<sub>2</sub> layer). The images were collected from the different areas of the same sample and reflect the gradual increase of the deposition rate of the precursor. The scale bars in panel a images correspond to 8 μm. (b) Optical image at 1000× magnification in polarized light of typical quasi-2D microbelt grown on Si wafer with 300 nm of SiO<sub>2</sub>. The characteristic labyrinth pattern of the ferroelastic domains manifests the existence of the elastic strain induced on the microbelt by the substrate upon cooling. (c) Optical image (1000×) in polarized light of the nearly complete VO<sub>2</sub> film formed on Si wafer with native oxide. Compared to that in panel b, the increased size of the ferroelastic domains reflects the reduction of the elastic strain. The scale bars in panels b and c correspond to 20 μm.



**Figure 2.** V–O temperature–composition phase diagram (based on data from ref 23 and 24). The evolution of the system described as motion of the figurative point along two distinct trajectories is shown as dark green and light green lines. The rate of the system evolution along the vertical direction is determined by the heating rate, while the horizontal one depends on the oxygen loss rate. The inset shows an enlarged area around the eutectic point at 670 °C. The optical microimages 1–12 demonstrate the morphology of a  $V_xO_y$  feature on the sample at few specific points of the V–O diagram along the slowest (dark green) of the synthesis routes.

drop-casted directly onto the sample. The stage was then sealed and evacuated, and the evolution of growth was directly observed through the sapphire window. This is the mode that was also used for templating experiments below. In external deposition (ED) mode, the precursor was delivered to the substrate by thermal evaporation from an external Pt microheater. In ED mode, the substrate temperature and deposition rate can be controlled independently.

**Reductive Growth.** Because of multiple oxidation states of vanadium, its oxides can have a variety of stable stoichiometries that are mutually transformable at specific temperatures and oxygen partial pressures, as reflected in the V–O temperature–composition phase diagram<sup>23,24</sup> in Figure 2. Therefore, the reductive growth of the  $VO_2$  nanostructures from the vanadia precursor appears to be a multistep process driven by the interplay between the kinetics of vanadia reduction and the thermodynamic stability of different phases. In the phase diagram shown, the vertical position of the system's figurative point is defined by temperature, whereas current oxygen content and ambient oxygen partial pressure control the figurative point in the horizontal direction. The V–O temperature–composition diagram in Figure 2 implies that the growth of  $VO_2$  nanowires does not necessarily require  $VO_2$  as a precursor. Moreover, vanadia impurities, which exist in generic  $VO_2$  material and/or the presence of an oxidizer can explain the growth of  $VO_2$  from a vanadium dioxide precursor at relatively low temperatures ( $T < T_m$ ). As per our microscopic optical observations, when the black powder of  $VO_2$  is heated

in a vacuum, the vast majority of the vanadium dioxide microparticles remain unchanged and only those orange microscopic impurity inclusions melt at *ca.* 700 °C and produce nanowires. The characteristic color and melting temperature imply that these are microparticles of vanadium pentoxide. Thus, vanadia microparticles serve as precursor for low-temperature synthesis of nanowires not only of the same stoichiometry but also of  $V_6O_{13}$  and  $VO_2$  through the process of thermal reduction.

The morphological and chemical evolution of the  $V_2O_5$  microparticles in the same area upon heating in low vacuum (residual oxygen pressure of about 0.5 Torr) is depicted in the right and top side optical images in Figure 2.

**Stage I:** Fine powder of vanadia is orange at room temperature (Figure 2, picture 1) but grows darker in color as the temperature rises, which indicates gradual chemical reduction<sup>25</sup> (powder retains dark color upon cooling and does not undergo significant change in grain size (see also Supporting Information S1).

**Stage II:** Being heated slowly, the precursor melts down at 670–682 °C (Figure 2, picture 4) forming small droplets that moderately wet  $SiO_2$  surfaces. Small microparticle aggregates melt congruently into microscopic droplets whose growth and decay obey the classical Ostwald ripening.<sup>26</sup> However, larger droplets always contain crystals of the guest phase(s). Under vacuum conditions (temperature being constant), crystallization of a new phase occurs in small droplets, too (Figure 2, picture 5–9). These newly formed crystalline nanowires of intermediate phase, identified as  $V_6O_{13}$  (see below), grow in size at the expense of the surrounding host liquid (Figure 2, picture 8–9), consuming it completely.

**Stage III:** Upon reaching 702 to 717 °C, the  $V_6O_{13}$  solid phase melts, as well (incongruently, Figure 2, picture 10) and  $VO_2$  nanowires finally crystallize from the secondary melt (Figure 2, picture 10–12). This final product of the described transformations can tolerate temperatures up to 1000 °C without changing its composition, as confirmed by XRD data (see Supporting Information S2).

The aforementioned growth scenario depends on heating rate and oxygen partial pressure. When high (*ca.* 500 °C/min) heating rate and low oxygen pressure (or vacuum) are employed (light green trajectory line in the Figure 2), congruent melting of the  $V_2O_5$  occurs at about 700 °C and no intermediate phase is observed.  $VO_2$  nanowires crystallize directly from the primary melt. Thus, depending on the interplay between the heating rate and oxygen pressure (and, to some extent, on the size of the precursor particles, which influences the rate of oxygen diffusion and loss), the figurative point takes different paths along the phase diagram. At low and moderate heating rates, the figurative point of the system first moves upward without shifting much horizontally (Figure 2, dark green line). Once in the

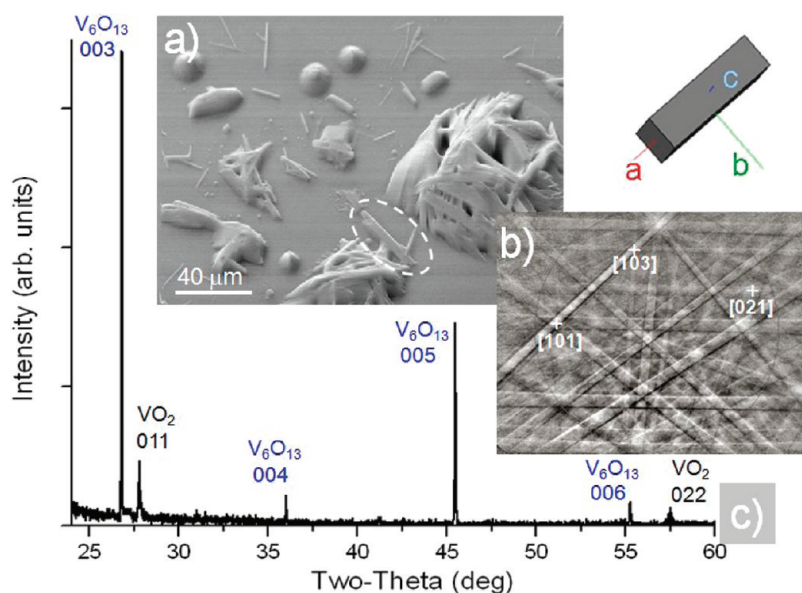


**Figure 3.** (a) SEM of micro/nanorods identified as the  $V_6O_{13}$  phase by EBSD and XRD, (b) EBSD pattern collected from the encircled microrod. The simulated crystallographic orientation of the  $V_6O_{13}$  unit cell (see inset in panel b) indicates that the microrod is elongated along the  $b$ -axis ([010] direction) and has (001) in-plane surface orientation. (c) XRD scan from this sample indexed to  $V_6O_{13}$  phase [PDF 89-0100] with minor inclusion of  $VO_2$  [PDF 72-0514]. The presence of only selected reflections for both oxides indicates that the nanostructures are single-crystalline with their corresponding crystal planes,  $\{001\}$  for  $V_6O_{13}$  and  $\{011\}$  for  $VO_2$ , being parallel to the substrate surface.

region of high temperatures, the system undergoes an increase in reduction rate and the point starts shifting to the left. Liquid phase appears when the point crosses the ( $V_2O_5 + V_6O_{13}$ ) solidus line and moves into the two-phase ( $V_6O_{13} + \text{melt}$ ) field (Figure 2, picture 4). Crystals of  $V_6O_{13}$  grow at the expense of the liquid until all liquid is consumed and the system enters the single phase (solid)  $V_6O_{13}$  field (Figure 2, picture 9).

**Characterization of the Intermediate Phases.** *Structural Characterization.* The intermediate states that correspond to pictures 6–9 in Figure 2 were further analyzed *ex situ* using X-ray diffraction (XRD) and electron backscattered diffraction (EBSD). The heating process was interrupted at the stage where newly formed nanostructures coexisted with the residual liquid phase (see Figure 2, pictures 8 and 9) and the sample was cooled down with a heating rate *ca.* 60 °C/s. We assume that the intermediate phase becomes preserved upon cooling. The corresponding SEM image in Figure 3a shows formation of partially agglomerated micro/nanorods. Local EBSD analysis identified them as  $V_6O_{13}$  single crystals (PDF file 89-0100) elongated in the [010] direction with (001) in-plane surface orientation (see Figure 3a,b). XRD in Figure 3c confirms that  $V_6O_{13}$  is the primary phase in this sample, with a small addition of  $VO_2$ . The presence of minute amounts of  $VO_2$  can be explained by possible temperature and compositional fluctuations in the sample, which enabled local equilibria to shift toward figurative points of pictures 10–12, Figure 2.

Further temperature rise brings the figurative point of picture 9, Figure 2, above the peritectic temperature

of 708 °C at which  $V_6O_{13}$  decomposes into solid  $VO_2$  and coexisting liquid (pictures 10–11, Figure 2). Upon further heating and oxygen loss, the system migrates toward the solid  $VO_2$  region (dark green line, Figure 2), which serves as the final destination of the system (picture 12, Figure 2). In the case of a high heating rate (light green line, Figure 2) the figurative point “travels” fast far above both solidus and liquidus and directly enters the liquid phase region. Owing to the fast temperature ramp and kinetic limitations, the supersaturation conditions favoring the formation of the  $V_6O_{13}$  phase do not hold for a sufficient enough time period and no intermediate phases are observed. As oxygen is rapidly lost at these high temperatures, the figurative point shifts to the left and crosses the liquidus, at which point  $VO_2$  crystals start to nucleate inside the liquid until the system’s figurative point finally terminates in the solid  $VO_2$  region on the phase diagram.

Similar to phase and structural analyses of samples containing the  $V_6O_{13}$  phase, sample 12 from Figure 2 was analyzed by XRD and EBSD. Both methods confirmed that nanorods, such as those in Figure 4a, were single crystals of the monoclinic  $VO_2$  phase. According to Figure 4a–c, the nanorods grow on  $SiO_2/Si$  in the [100] direction with their (011) top facet parallel to the substrate surface. This observation agrees with prior reports<sup>1,27</sup> and with our previous findings,<sup>21,22,28</sup> where  $VO_2$  nanorods had [100] growth axis and (011) top, (01 $\bar{1}$ ) side, and ( $\bar{2}01$ ) growth facets, respectively.<sup>20</sup> It should also be noted that for both intermediate (Figure 3) and final (Figure 4) stages of heat treatment,

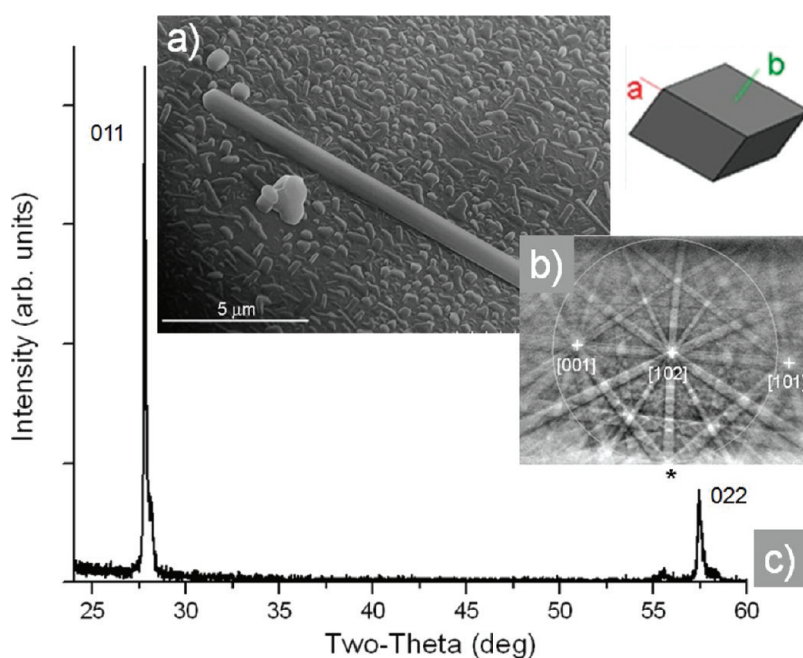


**Figure 4.** (a) SEM of the VO<sub>2</sub> nanorod, (b) corresponding EBSD pattern. The simulated crystallographic orientation of the VO<sub>2</sub> unit cell (inset above panel b) indicates that the nanorod is elongated along the *a*-axis ([100] direction) and has (011) in-plane surface orientation. (c) XRD scan from this sample indexed to VO<sub>2</sub> phase [PDF 72-0514]. Presence of only two reflections confirms that the nanorod (011) plane is parallel to the sample surface. Note: a low-intensity broad peak (\*) at  $2\Theta = 55.5^\circ$  could not be assigned unambiguously: while it matches ( $\bar{2}22$ ) or (220) reflections from VO<sub>2</sub>, no corresponding ( $\bar{1}11$ ) or (110) peaks were detected at low  $2\Theta$  angles.

the precipitated V<sub>6</sub>O<sub>13</sub> and VO<sub>2</sub> micro- and nanorods were randomly oriented on the amorphous SiO<sub>2</sub>/Si surface, which indicates their lack of epitaxial relationship to the substrate.

**Electronic Structure.** These structural analyses of the intermediate phases are supported by near edge X-ray absorption fine structure (NEXAFS) photoemission electron microscopy (PEEM) studies of the individual V<sub>x</sub>O<sub>y</sub> nano- and mesostructures conducted during the thermal excursion from room temperature up to *ca.* 1100 °C in UHV. Figure 5a–c shows PEEM images of the same area at three different temperatures of the Si sample with the native oxide layer covered with V<sub>2</sub>O<sub>5</sub> powder at room temperature. The field of view for all images was 75 μm, and they were recorded at the maximum absorption of V *L*-edge (518.7 eV). NEXAFS spectra at *L*-edge for V and *K*-edge for O, extracted from the PEEM image stack, are shown in Figure 5b and correspond to transitions from V spin–orbit split 2p<sub>3/2</sub>, 2p<sub>1/2</sub>, and corresponding O 1s states to unoccupied levels formed by hybridized O 2p and V 3d orbitals. In accordance with prior results (see most recent publications<sup>29–32</sup> and references therein), V *L*-edge spectra of V<sub>x</sub>O<sub>y</sub> samples in general exhibit two broad bands around 518 and 525 eV, and O *K* absorption has at least two main  $\pi^*$  and  $\sigma^*$  signatures originating from  $\pi$  and  $\sigma$  interactions of O 2p orbitals with corresponding V 3d orbitals.<sup>32</sup> Upon relatively fast annealing in UHV, corresponding to the light green figurative point path in Figure 2, melting of the vanadia microparticles

at around  $680 \pm 10^\circ\text{C}$  were observed, followed by the formation of VO<sub>2</sub> nanowires immersed in the liquid phase. Concomitant to the morphological changes, significant spectral evolution of the V 2p leading edge can be observed with temperature increase. As-deposited V<sub>2</sub>O<sub>5</sub> powder (A curve) has a distinctly resolved fine structure characteristic of multiple unoccupied V 3d–O 2p derived states in V<sub>2</sub>O<sub>5</sub>.<sup>33</sup> Upon annealing to *ca.* 750 °C, these features can be seen on the spectra from the nanowire NW2 (Figure 5a and B curve in Figure 5b). The latter implies that this VO<sub>2</sub> NW is still covered (or surrounded) by a thin layer of liquid phase. The degree of wetting depends on the stage of growth: for an example, the fine features at the V 2p<sub>3/2</sub> shoulder are absent in spectrum C collected from nanowire NW1, which exhibits characteristic VO<sub>2</sub> spectrum. At higher temperatures all nanostructures (*i.e.*, Figure 5b, NW1 curve D) show spectra typical of VO<sub>2</sub> single crystals.<sup>30</sup> This evolution of fine structure of the V 2p<sub>3/2</sub> shoulder with increased temperature manifests the decrease of the oxidation number of V and supports the aforementioned structural data. With regard to the O *K*-edge part of the NEXAFS spectra recorded on the same nanostructures during thermal annealing, under the constant incident angle and light polarization the ratio between  $\pi^*$  and  $\sigma^*$  bands changes with temperature, from  $\sigma^*$  prevailing for RT V<sub>2</sub>O<sub>5</sub> (curve A) and declining for VO<sub>2</sub> nanostructures at higher temperatures (curve C). The observed ratio trend is in qualitative agreement with the prior reports,<sup>30–32</sup> indicating the reduction of

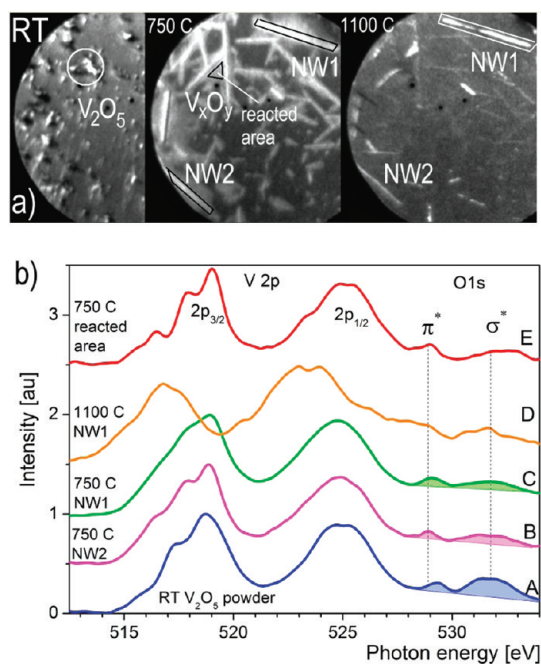


**Figure 5.** (a) XPEEM images of the evolution of morphology of  $V_2O_5$  powder recorded during thermal annealing in UHV. The middle and right panels show the nanowires in the intermediate ( $V_xO_y$ ) and final ( $VO_2$ ) phases. The selected regions denote the areas where NEXAFS spectra were collected. The photon energy for imaging was selected to be 518.7 eV; the field of view was  $75 \mu\text{m}$ . The temperature readings are approximate and might deviate from the actual temperature by up to  $50^\circ\text{C}$ . (b) Spectra A–D represent raw NEXAFS data acquired from the selected regions and individual nanowires in the vicinity of V 2p and O 1s edges at room temperature, 750, and  $1100^\circ\text{C}$ . The spectra were collected from the areas denoted in panel a and normalized to their maxima. The spectrum E was recorded from the reacted area (triangle in the middle panel) where liquid  $V_2O_5$  interacted with the  $SiO_2$  support. The shadowed bands highlight the change of the spectral weight of  $\sigma^*$  versus  $\pi^*$  bands with decrease of the V oxidation state.

vanadia upon sample heating, which also corroborates the changes in V 2p edge. The oxygen 1s band becomes low in intensity at higher temperatures (curve D), making it unsuitable for analysis. In summary, the observed spectroscopic changes indicate the reduction of the  $V_2O_5$  sample to  $VO_2$  and corroborate the above results on structural changes. From the chemical point of view, the discussed phase transformations can be described as thermal decomposition of specific vanadium oxides along the following routes:  $3 V_2O_5(l) \rightarrow V_6O_{13}(s) + O_2(g)$ ;  $2 V_6O_{13}(l) \rightarrow 12VO_2(s) + O_2(g)$ ; or overall  $2 V_2O_5(l) \rightarrow 4VO_2(s) + O_2(g)$  (where s, l, and g indexes stand for solid, liquid, and gas phase, correspondingly).

**Dynamics of the Growth and Crystal Morphologies.** Here we discuss a few important particularities of the growth mechanism of  $VO_2$  nanowires, nanobelts, and nanoplatelets made from  $V_2O_5$  precursor, which became apparent from *in situ* observations. Independent of the heating rate, the aforementioned reductive growth of  $VO_2$  nanostructures proceeds through a liquid phase. The oxygen partial pressure in the gas environment

and the heating rate define few possible growth scenarios with involvement of the intermediate phase (Figure 2). In addition, the ED or DD delivery modes of the precursor (*via* vapor phase or drop casted on the surface) at a given temperature determine the abundance of the material at the surface, the dimensions of the liquid droplets, and eventually the resultant nanostructure morphology.

In general, the equilibrium morphology of both the intermediate phase and final nano- and microstructures is described by the Wulff–Kaischew theorem<sup>34</sup> and depends on the surface energies of the free facets of the forming crystal and the interfacial energy at the support. During reductive growth, all of these parameters are dependent on the temperature and the oxygen content in the precursor droplets. Owing to strong interfacial interaction of the growing nanostructures, these thermodynamic considerations can account for the small thickness of our quasi-2D platelets: however, nucleation at preferred facets and/or kinetic considerations have to be invoked to describe one-dimensional growth.

During the thermal ramping in vacuum, large droplets of  $V_2O_5$  (formed from the precursor powder -DD mode) continuously lose oxygen and, as soon as sufficient supersaturation occurs, nucleation of  $V_6O_{13}$  solid phase takes place at the interface with silica. Crystalline nuclei grow inside the droplet along the direction perpendicular to the facet of minimal surface energy. Strong interfacial interaction with the substrate ensures in-plane growth of the  $V_6O_{13}$  nanowire. The diameter of the structure depends on the droplet size as well as on size of the initial nuclei, which in turn is controlled by the degree of supersaturation inside the host droplet. The growth rate depends on several (temperature dependent) processes:<sup>35</sup> (i) oxygen evaporation from the surface of the droplet; (ii) diffusion of oxygen and/or reduced species inside the droplet toward/from the surface and to the growing nuclei; (iii) interfacial interaction accompanied by solvation heat release, and (iv) dissipation of generated heat to the ambient.

When vanadia is delivered to a preheated (up to the  $V_2O_5$  melting point temperature) surface through the vapor phase (ED mode),  $V_2O_5$  nucleates in the form of immobile microdroplets that grow *via* the Ostwald ripening. Some of the vanadia droplets contain heterogeneous nucleation sites (*i.e.*, surface defects) and, if there be a slight supercooling, develop crystal nuclei of  $V_2O_5$ . These grow one-dimensionally, first inside the droplet at the interface with the substrate and eventually beyond the host droplet (Figure 6). At higher temperatures, at which vanadia NW melts, the growing depletion of the microdroplet with initial stoichiometry of  $V_2O_5$  of oxygen leads to supersaturation of the  $V_6O_{13}$  phase. Similar to the aforementioned scenario, the  $V_6O_{13}$  guest phase nucleates and grows as a single-crystal nanostructure inside the droplet, except that in

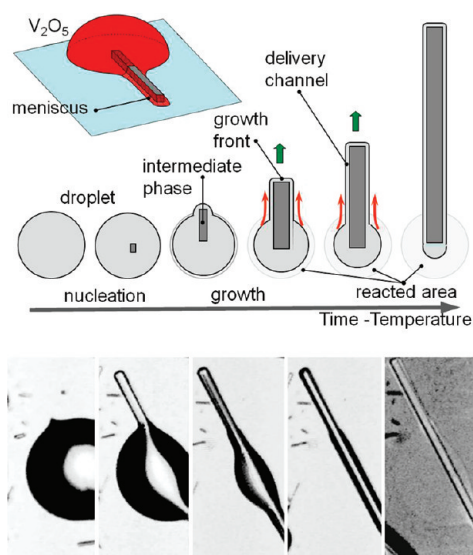


**Figure 6.** Wetting assisted growth of  $V_xO_y$  nanostructures. Top panel: the nucleation and evolution of a nanostructure inside the precursor droplet. The growth front is located on top of the nanostructure, where material is delivered from the host droplet *via* side wetting channels. The precursor droplet partly dissolves the oxide substrate at high temperature, leaving noticeable traces. Bottom panel: set of *ca.*  $10 \times 25 \mu\text{m}^2$  consequent optical micrographs of the individual droplet and the  $VO_2$  NW evolving from it during slow heating.

this case the crystal is formed from the solution, rather than from the melt.

**Wetting Layer Assisted Growth.** It is the presence of the liquid phase that promotes in-plane growth of the quasi-1D nanostructures on a variety of tested substrates ( $\text{SiO}_2/\text{Si}$ , Si with native oxide layer,  $\text{Si}_3\text{N}_4$ , quartz, GaN,  $\text{TiO}_2$ , etc.) and is responsible for the material delivery mechanism to the growing front. There are two driving forces favoring this growth regime (Figure 6): (i) significant interfacial interaction of the single-crystal  $V_xO_y$  (or nuclei) with the substrate at elevated temperatures, which in many cases results in epitaxial growth (see below) and (ii) capillary forces induced by the liquid phase and acting along the interface between the growing nanostructure and the substrate. During nanostructure growth from the host droplet, a thin liquid film wets the nanostructure along its entire length, creating a material delivery channel for the NW growing front (Figure 6, top panel). Owing to strong interfacial interaction with the aforementioned supports, droplets are immobile on the surface and do not act as growth fronts, which is different from the standard VLS growth mode. Instead, the growth takes place in the developing apex of the nanowire, and feeding material is delivered to the growing tip of the nanowires *via* the peripheral (*i.e.*, nanowire sidewall) liquid wetting layer (see Figure 6, bottom panel). It is necessary to note that the precursor droplet partly dissolves the oxide substrate at high temperature, leaving noticeable traces after it is

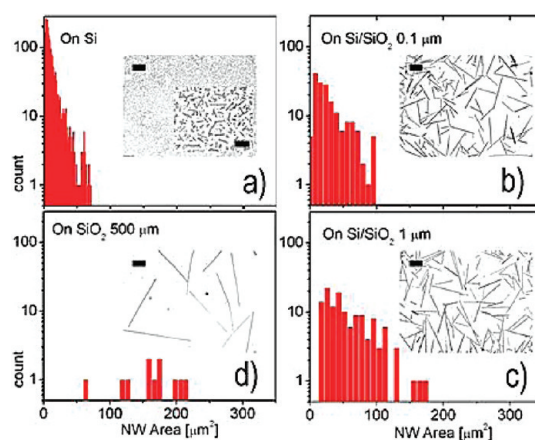


**Figure 7.** Histograms of the size and density distribution of nanostructures grown on substrates with four different  $\text{SiO}_2$  layer thicknesses. Pictures are optical images of corresponding substrates (grayscale, background removed). Scale bars are  $100 \mu\text{m}$ , except for the zoomed-in area of the silicon substrate, where it is  $30 \mu\text{m}$ .

completely consumed by evaporation and nanowire feeding (see bottom right panel, Figure 6 and discussion below).

**The Importance of the Interfacial Layer.** These interfacial effects have been reported in prior works and were found to be responsible for the “sinking” of the  $VO_2$  nanorods in thick  $\text{SiO}_2$  layer and some other substrates.<sup>2–4,12,36</sup> In our case, for comparative studies of the influence of support materials on the growth of  $VO_2$  nanowires the different substrates (silicon with native oxide layer, silicon with thermal oxide layer of 100 and 1000 nm, and quartz) with sizes *ca.* 20 to 60  $\text{mm}^2$  have been placed side-by-side in the tube furnace and used to grow  $VO_2$  NWs. The optical images of representative areas of these substrates were compared and analysis of the morphology of the grown nanowires was performed using particle analysis software (ImageJ). It was found that quartz promotes the growth of nanowires more than any other silicon dioxide-based substrate, leading to millimeter-long structures. This growth-promoting influence was observed by us many times and is summarized in Figure 7. As can be seen, the aspect ratio of the nanowires changes significantly as the oxide thickness increases: from very densely packed, few-micrometer-long rods on Si with a native oxide layer (Figure 7a), to nanowires of 100–400  $\mu\text{m}$  in length on  $\text{Si}/\text{SiO}_2$  (Figure 7b,c) to near millimeter long (but low surface density) mesowires on quartz (Figure 7d). More quantitatively, this can be seen from the particle-size distribution analysis where the shift of the average nanostructure area to larger values is mainly due to nanowire length increase. It implies that the nucleation rate is highest but growth rate lowest on silicon, whereas the opposite trend is observed for quartz. Most of the  $V_2O_5$  droplets that initially appear on quartz do not form crystal nuclei during heating and simply evaporate (without thermal

decomposition) from the surface later on when the temperature rises. This phenomenon can be understood in the light of the  $V_2O_5$ – $SiO_2$  phase diagram,<sup>37</sup> which indicates that within the temperature region of interest (i) the two substances do not form any chemical compounds with each other; (ii) silica has limited solubility in molten vanadia; and (iii) the eutectic of the two compounds (*ca.* 1 wt % of  $SiO_2$ ) has a melting point about 20° lower than  $V_2O_5$ . The formation of these eutectic (reactive) areas can be seen in the optical images in Figure 6 (bottom right panel) and as the brighter area around the nanowires in PEEM images in Figure 5. The early microscopy studies of such reactive traces at the droplet–substrate molten interface can be found in refs 38 and 39. The NEXAFS spectrum of such eutectic areas (curve E, Figure 5) corroborates with the chemical composition being close to  $V_2O_5$ . Thus, one-dimensional growth, in addition to the aforementioned factors, is also promoted by the “dissolving action” of molten vanadia as it (i) dissolves the silica layer *ca.* 100 nm underneath and around the growing nanowire and (ii) creates the channel for NW to grow and activates the delivery of the material to the growing front at the apex of the nanowire. Since no chemical compound is formed in this process, the liquid vanadia transforms into  $VO_2$  at later stages of the annealing, while dissolved silica precipitates from the saturated solution, leaving visible traces on the surface and firmly “glueing” the nanostructures to the substrate ( $VO_2$ – $SiO_2$  eutectic melts at *ca.* 1350 °C).

When the thickness of the silica layer is less than *ca.* 100 nm, the eutectic may interact with the core substrate, according to (Si-assisted reduction):  $2 V_2O_5(l) + Si(s) \rightarrow 4VO_2(s) + SiO_2$  (solution), and a high density of stable, immobile, small-aspect-ratio  $VO_2$  nuclei are preferentially formed (as reaction products) that evolve into short rods, small platelets, or film upon further precursor deposition (Figures 7a and 1a,c).

*“Fuel Station” Mechanism of Growth of the Ultralong NWs and Formation of Quasi-2D Platelets.* When the average distance between adjacent microdroplets is large (lateral density is low) the nanostructure, growing *via* this wetting layer-assisted growth mechanism, eventually uses up all the host droplet’s material and halts its growth. At high lateral density of the microdroplets, the growing nanowire eventually hits the neighboring microdroplet before the host droplet becomes depleted. Once the NW tip touches the next droplet, capillary forces spread some of the new liquid along the NW sidewalls and new material is used in further NW lengthening (Figure 8a–d). This “fuel station” (FS) growth mechanism explains the growth of extremely long nanowires whose length can reach a few millimeters.

As mentioned earlier, the large aspect ratio of the NWs stems from the constrained character of the growth, different from the shape at thermodynamic equilibrium. If growth conditions are changed so that they approach equilibrium, the growth morphology must change too and the length/width ratio will go closer to unity. Should a growing NW encounter a droplet of size much larger than its width, the growth mode changes, and retaining almost the same length, the NW significantly widens, forming a wide platelet (as seen in Figure 1b [see also Supporting Information section S3, video 1]). Thus, the abundance of available liquid material somewhat resembling that of the case of unconstrained growth brings about a change in apparent morphology: from quasi-1D NW to 2D nanobelt (platelet). In cases where there is no significant lateral spreading of the droplet (poor wetting), one-dimensional growth prevails. All the described peculiar behavior was observed for both  $V_2O_5$  and  $V_6O_{13}$  phases (see Supporting Information videos 1 and 2). Our observations confirm the propensity of vanadium pentoxide droplets to remain liquid at temperatures lower than its melting point for sufficient time due to the supercooling effect,<sup>10</sup> until a NW network grows by

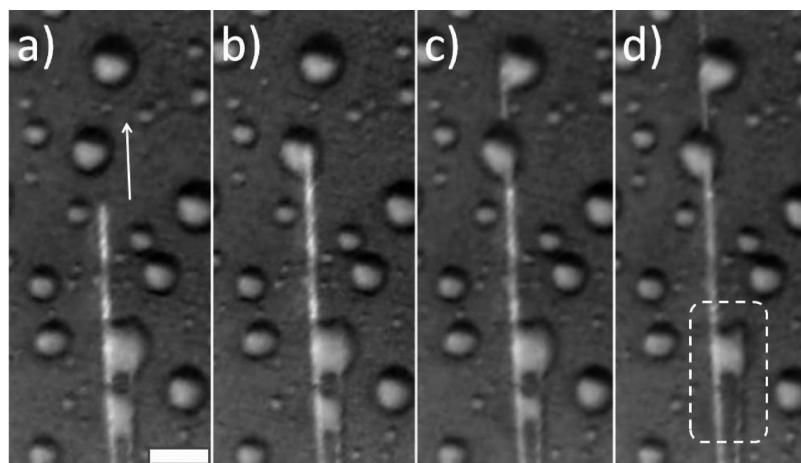


**Figure 8.** Optical images of growing nanowire that uses the liquid droplets as a new source of material (“fuel stations”). The dashed area exemplifies the depletion of the droplets. For details, see text. The scale bar is 10  $\mu$ m.

the “fuel station” mechanism and consumes them all. The melting point of this network’s material suggests that it comprises  $V_2O_5$  NWs. Thus, during the first stage of ED mode growth, the FS mechanism combines with simple recrystallization due to the low temperature, producing structures of roughly the same stoichiometry as the liquid from which they evolved.

**Epitaxial Growth and Templating.** The observed particularities of  $VO_2$  NW growth can be used to control the  $V_xO_y$  nanostructure morphology, surface location, orientation, composition, and other properties (e.g., strain) for bottom-up device fabrication.

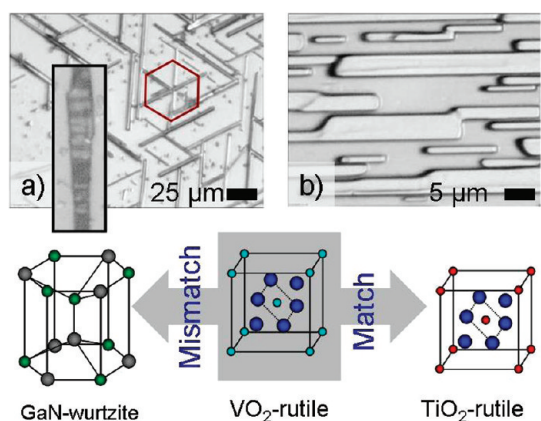


Figure 9. Epitaxy:  $VO_2$  nanowires grown on c-cut of GaN and (110)  $TiO_2$ . (a) Mismatch of GaN and  $VO_2$  lattices gives rise to triangular and hexagonal patterns, as well as to the presence of ferroelastic domains in individual NWs (left panel inset). (b) The small difference between the lattice constants and atomic radii of V and Ti leads to perfect alignment of  $VO_2$  NWs along one axis and absence of stress-induced domains.

Directed growth of the  $VO_2$  nanowires *via* epitaxial relations with substrates was reported earlier<sup>36,40–42</sup> and in our case was realized on (0001) GaN and  $TiO_2$  (110) surfaces. As can be seen (Figure 9), the direction of NW growth complies with the crystallographic symmetry of the surfaces: (i) hexagonal symmetry in  $VO_2$  nanowire surface growth orientation can be observed on wurtzite-type GaN, which is expected for GaN c-plane (Figure 9a) and, on the other hand, (ii) perfect alignment of NWs along (001) direction can be seen in Figure 9b.

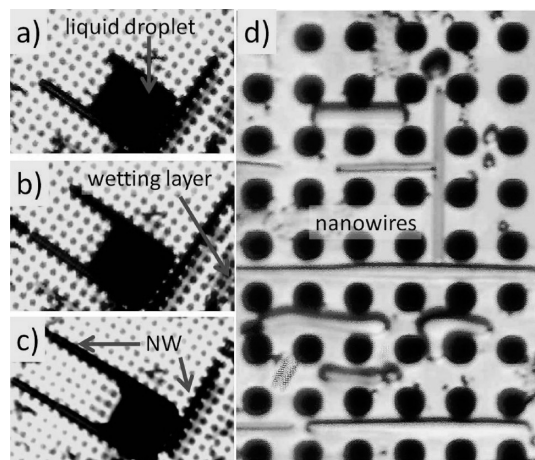


Figure 11. (a–c) Sequential optical microscope images of the perforated SiN membrane with  $V_2O_5$  droplet (black area). Owing to the wetting of the substrate, the droplet and growing nanostructures adopt discrete shapes and growth directions; (d) large-magnification optical image (1000 $\times$ ) of the resultant  $VO_2$  nanostructures grown on a perforated membrane. The hole diameter is 2  $\mu m$ .

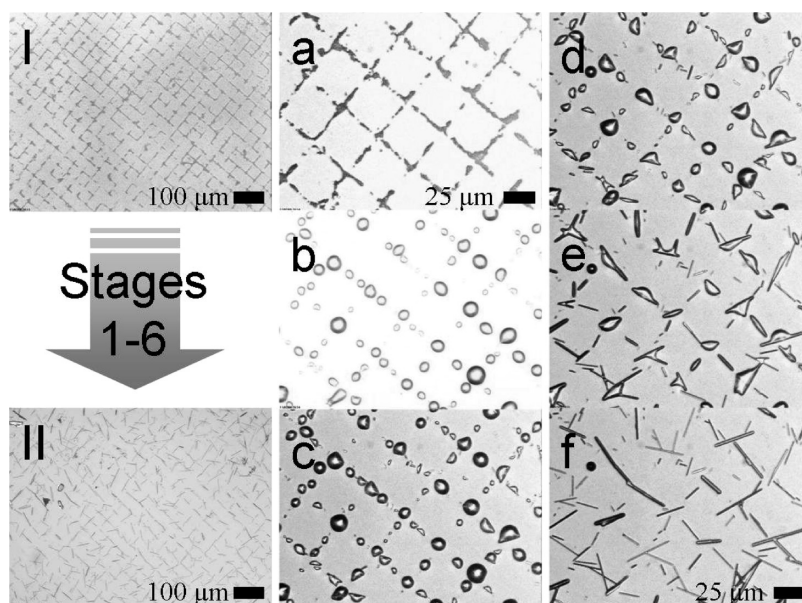


Figure 10. Templating: pattern created by deposited precursor powder remains after synthesis as the grown nanowires line up along the axes of maximum precursor content. Large-scale morphology of the initial deposit I (powder) and final II nanowires are shown in the left column. The detailed evolution of the deposit during annealing in low vacuum is depicted in the panels a–f.

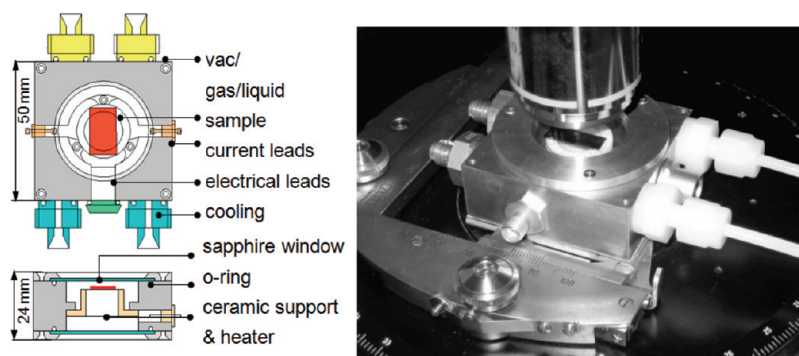


Figure 12. Left panel: Schematic design of the hot stage. The heating element and growth substrate is a Si/SiO<sub>2</sub> wafer that can be heated up to 1000 °C. Right panel: hot stage attached to rotatable table of Nikon L150 upright microscope. Long working distance of the CFI60 optics allows *in situ* observations with magnification up to 1000 $\times$ .

Since the formation of ferroelastic domains is indicative of the presence of elastic strain in the VO<sub>2</sub> nanostructure, this can be used as a marker of the lattice misfit or significant difference between thermal expansion coefficients. Imaging of the nanostructures in polarized light revealed no ferroelastic domains in VO<sub>2</sub> structures grown on titania, while NWs grown on GaN indicated the presence of stress, which corroborates with significant lattice misfit in the latter case. It should be noted that in the case of titania the crystal miscut can create preferable nucleation sites along the step edges as well. One can notice that liquid droplets formed during DD synthesis completely wetted the surfaces of TiO<sub>2</sub> and GaN (not forming individual droplets), which indicates strong interfacial interaction between liquid and GaN (TiO<sub>2</sub>) surfaces.

To go beyond widely studied vanadia epitaxial and oriented growth (see recent reviews<sup>43,44</sup> and references therein), we tested several alternative templating techniques to control the positions and orientations of VO<sub>2</sub> nanostructures. These were: (a) surface patterning with precursor powder and (b) templating against a microstructured substrate. The first approach is shown in Figure 10. A suspension of fine powdered vanadia in acetone was drop-casted onto the Si/SiO<sub>2</sub> wafer surface through a shadow mask (DD mode). Owing to the meniscus formation between the mesh and the substrate and following drying of suspension, the material was concentrated by the bars of the mesh, thus creating a square pattern on the substrate (Figure 10a). During annealing (up to 1000 °C, high heating rate) the morphology of the deposit followed the aforementioned reductive growth, and molten droplets perfectly followed the predeposited pattern (Figure 10b-f). The templating can be interrupted at any stage to obtain V<sub>6</sub>O<sub>13</sub> or VO<sub>2</sub> nanowires. A significant fraction of the NWs grow from droplets along the predesigned pattern following the preferable material's supply direction.

The existence of the intermediate liquid phase during V<sub>x</sub>O<sub>y</sub> nanostructure growth opens an alternative

route to control the growth direction employing capillary effect. Manipulating the capillary forces *via* micropatterning, one can guide the growth of the nanostructures in the desired direction. This approach was implemented using commercial silicon nitride perforated membranes as substrates. Confinement of the wetting layer and precursor liquid between the perforations guides the growth of the NWs along the two perpendicular axes (Figure 11).

## CONCLUSIONS AND OUTLOOK

We found that use of V<sub>2</sub>O<sub>5</sub> as a precursor for VO<sub>2</sub> nanostructure reductive growth is a simple and relatively low temperature route to obtaining quasi-1 or -2D nanostructures or thin films on variety of substrates. This method can be applied to a number of reducible metal oxides which suboxides have lower melting temperature. However, this synthesis is a complex process that, in general, proceeds *via* multiple phase transformations and compositionally different phases (*i.e.*, the growth of the intermediate V<sub>6</sub>O<sub>13</sub> nanowires).

The key factors governing the growth process are the abundance of the precursor on the surface, its temperature, the affinity of liquid droplets to the substrate, and the competition between oxygen loss (if in vacuum or a reductive atmosphere) and heating rates. Employing the balance between the aforementioned parameters, the chemical composition, morphology, and size of the final structures can be tuned, providing a strategy that can be used to control the growth of the desired nanostructures or films. Along these lines we find the following:

Using a heating rate that is lower than the rate of vanadia reduction allows the growth process to be interrupted at a desired intermediate stage and to obtain nanostructures of V<sub>2</sub>O<sub>5</sub>, V<sub>6</sub>O<sub>13</sub>, or VO<sub>2</sub>.

Favoring the conditions for the "fuel station" growth mechanism, one can obtain ultralong nanowires of vanadium oxides. Alternatively, increasing the amount of precursor on the surface (with other parameters in tune) favors the formation of 2D platelets.

Through the manipulation of the liquid phase, its eutectic formation with the substrate material (*i.e.*, in case of  $V_2O_5$ – $SiO_2$  system) and by utilizing the wetting assisted growth mechanism in particular, one can obtain a variety of final morphologies of nanowires and films by harnessing capillary forces and fine-tuning

the affinity of the substrate or its shape or lateral patterning.

Finally, one can envision that epitaxial growth can be used to influence the structural/mechanical, optical, and electrical properties of the final nanostructures, which can be exploited in nanodevice fabrication.

## METHODS

For *in situ* microscopy studies, we designed a compact microscope hot stage (temperature up to *ca.* 1000 °C) (Figure 12) coupled with a long working distance and high magnification (up to 1000 $\times$ ) upright Nikon L150 microscope. The hot stage's cavity is isolated from the environment with a 1 mm thick sapphire optical window and houses a rectangular (5 mm  $\times$  15 mm) heater/substrate cut from a commercial Si/SiO<sub>2</sub> wafer. DC current was passed through this heavily doped Si substrate, and Joule heat was used to control the temperature of the growth zone. The substrate requires *ca.* 30 to 40 W for its central region to reach 1000 °C. The stage is equipped with a miniature thermocouple, which could be attached to the region of interest, thus allowing local temperature measurements. Heat dissipation into the environment was minimized by using an internal thermal shielding and a water-cooled body of the cell. Both ED and DD growth experiments have been realized inside the hot stage. Complementary growth experiments have been conducted in a tube furnace for comparison (see ref 6 for growth conditions details). Off-the-shelf VO<sub>2</sub> fine powder (99.6% Alfa Aesar) or its mixtures with V<sub>2</sub>O<sub>5</sub> powder (the same vendor) (up to 12 wt % in VO<sub>2</sub>) were used as source material, and the deposition rate inside the tube furnace was regulated by changing the distance between the substrate and the source in the 0–5 mm range.

Different substrates, Si with native oxide layer, SiO<sub>2</sub> with thermal oxide layer of 100 and 1000 nm (University Wafer), quartz (Ted Pella), rutile TiO<sub>2</sub> (110)-cut (Princeton Scientific Corp.), and GaN *c*-plane cut and perforated SiN membranes (Aquamarijn Micro Filtration BV), with sizes of *ca.* 20–60 mm<sup>2</sup> and thickness of 200–600  $\mu$ m were used in this study. Before the experiment the samples were sonicated (except SiN membranes) for a few minutes in isopropyl alcohol and air-dried. No additional surface pretreatment was used.

For comparative *ex situ* studies of the samples' morphology at different growth stages, a Hitachi S-4700 field emission scanning electron microscope (FESEM) was used. The identification of phases and analysis of structural quality and crystallographic orientations of micro- and nanostructures were performed by XRD and EBSD. The XRD spectra were collected using a Bruker-AXS D8 scanning X-ray microdiffractometer equipped with a general area detector diffraction system (GADDS) using Cu K $\alpha$  radiation. (The two-dimensional 2 $\theta$ - $\Omega$  GADDS patterns were angular-integrated to produce standard "intensity-2 $\theta$ " spectra.) The EBSD patterns were recorded using an HKL Nordlys II EBSD detector attached to the Hitachi S-4700 microscope.

To complement the optical studies, the near surface change of the chemical composition of the V<sub>x</sub>O<sub>y</sub> nanostructures as a function of temperature PEEM-NEXAFS measurements were carried out at the Canadian Light Source (CLS) on a soft X-ray spectromicroscopy (SM) beamline.<sup>45</sup> During this study an Elmitec PEEM-III microscope capable of delivering spectroscopic as well as microscopic information at submicrometer-resolution scale<sup>46</sup> was used. Photons were incident at a shallow 16 degrees angle to the sample surface making the PEEM measurements more surface sensitive. PEEM images were collected as a function of temperature during photon energy scans around V 2p and O 1s edges. The monochromator resolution with 50  $\mu$ m exit slits is better than 0.1 eV in the region of interest. V<sub>2</sub>O<sub>5</sub> powder on the Si wafer was heated from room temperature up to 1100 °C in a UHV chamber with a base pressure lower than 2  $\times$  10<sup>-9</sup> Torr.

**Disclosure:** Commercial equipment and material suppliers are identified in this paper to adequately describe experimental procedures. This does not imply endorsement by NIST.

**Acknowledgment.** The research was funded through NSF ECCS-0925837 and SISGR-DOE ERKCM67 grants. PEEM-NEXAFS measurements were performed at the Canadian Light Source, which is supported by the NSERC, NRC of Canada, the Canadian Institutes of Health Research, the Province of Saskatchewan, Western Economic Diversification Canada, and the University of Saskatchewan. The authors also highly appreciate the careful reading and valuable suggestions made by M. L. Wilshaw-Watts and by D. Josell of NIST.

**Supporting Information Available:** S1: Analysis of the vis–IR spectra taken from a sample patch during its reduction in a vacuum on the hot stage. S2: XRD spectra of the samples annealed in a tube furnace at certain temperatures showing structural phase transformations. S3: pictorial explanation of the DD and ED growth modes. S4: a video showing growth of a V<sub>2</sub>O<sub>5</sub> NW by FS mechanism. S5: a video showing growth of a V<sub>2</sub>O<sub>5</sub> mesobelt. This material is available free of charge *via* the Internet at <http://pubs.acs.org>.

## REFERENCES AND NOTES

- Guiton, B. S.; Gu, Q.; Prieto, A. L.; Gudixsen, M. S.; Park, H. Single-Crystalline Vanadium Dioxide Nanowires with Rectangular Cross Sections. *J. Am. Chem. Soc.* **2005**, *127*, 498–499.
- Baik, J. M.; Kim, M. H.; Larson, C.; Wodtke, A. M.; Moskovits, M. Nanostructure-Dependent Metal-Insulator Transitions in Vanadium–Oxide Nanowires. *J. Phys. Chem. C* **2008**, *112*, 13328–13331.
- Wu, J. Q.; Gu, Q.; Guiton, B. S.; de Leon, N. P.; Lian, O. Y.; Park, H. Strain-Induced Self Organization of Metal-Insulator Domains in Single-Crystalline VO<sub>2</sub> Nanobeams. *Nano Lett.* **2006**, *6*, 2313–2317.
- Wei, J.; Wang, Z. H.; Chen, W.; Cobden, D. H. New Aspects of the Metal-Insulator Transition in Single-Domain Vanadium Dioxide Nanobeams. *Nat. Nanotechnol.* **2009**, *4*, 420–424.
- Kam, K. C.; Cheetham, A. K. Thermochromic VO<sub>2</sub> Nanorods and Other Vanadium Oxides Nanostructures. *Mater. Res. Bull.* **2006**, *41*, 1015–1021.
- Strelcov, E.; Lilach, Y.; Kolmakov, A. Gas Sensor Based on Metal-Insulator Transition in VO<sub>2</sub> Nanowire Thermistor. *Nano Lett.* **2009**, *9*, 2322–2326.
- Cao, J.; Fan, W.; Zheng, H.; Wu, J. Thermoelectric Effect across the Metal-Insulator Domain Walls in VO<sub>2</sub> Microbeams. *Nano Lett.* **2009**, *9*, 4001–4006.
- Lu, W.; Lieber, C. M. Semiconductor Nanowires. *J. Phys. D, Appl. Phys.* **2006**, *39*, R387–R406.
- Maeng, J.; Kim, T. W.; Jo, G.; Lee, T. Fabrication, Structural and Electrical Characterization of VO<sub>2</sub> Nanowires. *Mater. Res. Bull.* **2008**, *43*, 1649–1656.
- Kim, M. H.; Lee, B.; Lee, S.; Larson, C.; Baik, J. M.; Yavuz, C. T.; Seifert, S.; Vajda, S.; Winans, R. E.; Moskovits, M.; *et al.* Growth of Metal Oxide Nanowires from Supercooled Liquid Nanodroplets. *Nano Lett.* **2009**, *9*, 4138–4146.
- Wriedt, H. The O–V (Oxygen–Vanadium) System. *J. Phase Equilib.* **1989**, *10*, 271–277.

12. Cheng, Y.; Wong, T. L.; Ho, K. M.; Wang, N. The Structure and Growth Mechanism of VO<sub>2</sub> nanowires. *J. Cryst. Growth* **2009**, *311*, 1571–1575.
13. Wu, Y. Y.; Yang, P. D. Direct Observation of Vapor–Liquid–Solid Nanowire Growth. *J. Am. Chem. Soc.* **2001**, *123*, 3165–3166.
14. Kodambaka, S.; Tersoff, J.; Reuter, M. C.; Ross, F. M. Germanium Nanowire Growth below the Eutectic Temperature. *Science* **2007**, *316*, 729–732.
15. Prikhodko, S. V.; Sitzman, S.; Gambin, V.; Kodambaka, S. *In Situ* Electron Backscattered Diffraction of Individual GaAs Nanowires. *Ultramicroscopy* **2008**, *109*, 133–138.
16. Lang, C.; Kodambaka, S.; Ross, F. M.; Cockayne, D. J. H. Real Time Observation of GeSi/Si(001) Island Shrinkage Due to Surface Alloying During Si Capping. *Phys. Rev. Lett.* **2006**, *97*.
17. Gai, P. L. Developments in *in Situ* Environmental Cell High-Resolution Electron Microscopy and Applications to Catalysis. *Top. Catal.* **2002**, *21*, 161–173.
18. Jung, I.; Pelton, M.; Piner, R.; Dikin, D. A.; Stankovich, S.; Watcharotone, S.; Hausner, M.; Ruoff, R. S. Simple Approach for High-Contrast Optical Imaging and Characterization of Graphene-Based Sheets. *Nano Lett.* **2007**, *7*, 3569–3575.
19. Turnbull, D.; Cech, R. E. Microscopic Observation of the Solidification of Small Metal Droplets. *J. Appl. Phys.* **1950**, *21*, 804–810.
20. Brenden, B. B.; Newkirk, H. W.; Bates, J. I. Principles of High-Temperature Microscopy. *J. Am. Ceram. Soc.* **1960**, *43*, 246–251.
21. Tselev, A.; Strelcov, E.; Luk'yanchuk, I. A.; Budai, J. D.; Tischler, J. Z.; Ivanov, I. N.; Jones, K.; Proksch, R.; Kalinin, S. V.; Kolmakov, A. Interplay between Ferroelastic and Metal-Insulator Phase Transitions in Strained Quasi-Two-Dimensional VO<sub>2</sub> Nanoplatelets. *Nano Lett.* **2010**, *10*, 2003–2011.
22. Tselev, A.; Meunier, V.; Strelcov, E.; Shelton, W. A.; Luk'yanchuk, I. A.; Jones, K.; Proksch, R.; Kolmakov, A.; Kalinin, S. V. Mesoscopic Metal-Insulator Transition at Ferroelastic Domain Walls in VO<sub>2</sub>. *ACS Nano* **2010**, *4*, 4412–4419.
23. Kosuge, K. The Phase Diagram and Phase Transition of the V<sub>2</sub>O<sub>3</sub>–V<sub>2</sub>O<sub>5</sub> System. *J. Phys. Chem. Solids* **1967**, *28*, 1613.
24. Wriedt, H. A. The O–V (Oxygen–Vanadium) System. *Bull. Alloy Phase. Diagrams* **1989**, *10*, 271.
25. Yuan, N. Y.; Li, J. H.; Lin, C. L. Valence Reduction Process from Sol-Gel V<sub>2</sub>O<sub>5</sub> to VO<sub>2</sub> Thin Films. *Appl. Surf. Sci.* **2002**, *191*, 176–180.
26. Ostwald, W. *Lehrbuch der Allgemeinen Chemie*; Wilhelm Engelmann: Leipzig, Germany, 1896.
27. Chou, J. Y.; Lensch-Falk, J. L.; Hemesath, E. R.; Lauhon, L. J. Vanadium Oxide Nanowire Phase and Orientation Analyzed by Raman Spectroscopy. *J. Appl. Phys.* **2009**, *105*.
28. Tselev, A.; Luk'yanchuk, I. A.; Ivanov, I. N.; Budai, J. D.; Tischler, J. Z.; Strelcov, E.; Kolmakov, A.; Kalinin, S. V. Symmetry Relationship and Strain-Induced Transitions between Insulating M1 and M2 and Metallic R Phases of Vanadium Dioxide. *Nano Lett.* **2010**, *10*, 4409–4416.
29. Brik, M. G.; Ogasawara, K.; Ikeno, H.; Tanaka, I. Fully Relativistic Calculations of the L-2,L-3-Edge XANES Spectra for Vanadium Oxides. *Eur. Phys. J. B* **2006**, *51*, 345–355.
30. Ruzmetov, D.; Senanayake, S. D.; Ramanathan, S. X-ray Absorption Spectroscopy of Vanadium Dioxide Thin Films Across the Phase-Transition Boundary. *Phys. Rev. B* **2007**, *75*.
31. Havecker, M.; Cavalleri, M.; Herbert, R.; Follath, R.; Knop-Gericke, A.; Hess, C.; Hermann, K.; Schlögl, R. Methodology for the Structural Characterisation of V<sub>x</sub>O<sub>y</sub> Species Supported on Silica Under Reaction Conditions by Means of *in Situ* O K-Edge X-ray Absorption Spectroscopy. *Phys. Stat. Sol. B* **2009**, *246*, 1459–1469.
32. Velazquez, J. M.; Jaye, C.; Fischer, D. A.; Banerjee, S. Near Edge X-ray Absorption Fine Structure Spectroscopy Studies of Single-Crystalline V<sub>2</sub>O<sub>5</sub> Nanowire Arrays. *J. Phys. Chem. C* **2009**, *113*, 7639–7645.
33. Goering, E.; Muller, O.; Klemm, M.; denBoer, M. L.; Horn, S. Angle Dependent Soft-X-ray Absorption Spectroscopy of V<sub>2</sub>O<sub>5</sub>. *Philos. Mag. B* **1997**, *75*, 229–236.
34. Markov, I. V. *Crystal Growth for Beginners: Fundamentals of Nucleation Growth and Epitaxy*, 2 ed.; World Scientific: Singapore, 2003; p 546.
35. Kirkpatrick, R. J. Crystal-Growth from Melt—Review. *Am. Mineral.* **1975**, *60*, 798–814.
36. Sohn, J. I.; Joo, H. J.; Porter, A. E.; Choi, C. J.; Kim, K.; Kang, D. J.; Welland, M. E. Direct Observation of the Structural Component of the Metal-Insulator Phase Transition and Growth Habits of Epitaxially Grown VO<sub>2</sub> Nanowires. *Nano Lett.* **2007**, *7*, 1570–1574.
37. Gravette, D. B.; Barrett, L. R. An Investigation of the System V<sub>2</sub>O<sub>5</sub>–SiO<sub>2</sub>. *Trans. Brit. Ceram. Soc.* **1966**, *65*, 199–203.
38. Grinberg, S. A.; Givargizov, E. I. Movement of Drops of Germanium–Gold Alloy along Germanium Surface under Action of a Temperature Gradient. *Kristallografiya* **1973**, *18*, 380–384.
39. Swiech, W.; Bauer, E.; Mundscha, M. A Low-Energy Electron-Microscopy Study of the System Si(111)–Au. *Surf. Sci.* **1991**, *253*, 283–296.
40. Gao, W.; Wang, C. M.; Wang, H. Q.; Henrich, V. E.; Altman, E. I. Growth and Surface Structure of Vanadium Oxide on Anatase (001). *Surf. Sci.* **2004**, *559*, 201–213.
41. Muraoka, Y.; Hiroi, Z. Metal-Insulator Transition of VO<sub>2</sub> Thin Films Grown on TiO<sub>2</sub> (001) and (110) Substrates. *Appl. Phys. Lett.* **2002**, *80*, 583–585.
42. Sambri, M.; Sangiovanni, G.; Granozzi, G.; Parmigiani, F. Growth and the Structure of Epitaxial VO<sub>2</sub> at the TiO<sub>2</sub>(110) Surface. *Phys. Rev. B* **1997**, *55*, 7850–7858.
43. Nag, J.; Haglund, R. F. Synthesis of Vanadium Dioxide Thin Films and Nanoparticles. *J. Phys. Cond. Matter* **2008**, *20*.
44. Surnev, S.; Ramsey, M. G.; Netzer, F. P. Vanadium Oxide Surface Studies. *Prog. Surf. Sci.* **2003**, *73*, 117–165.
45. Kaznatcheev, K. V.; Karunakaran, C.; Lanke, U. D.; Urquhart, S. G.; Obst, M.; Hitchcock, A. P. Soft X-ray Spectromicroscopy Beamline at the CLS: Commissioning Results. *Nucl. Instr. Methods A* **2007**, *582*, 96–99.
46. Lanke, U.; Hitchcock, A.; Urquhart, S. The Photoemission Electron Microscope at the Canadian Light Source: An Overview. *Canadian Light Source Activity Report*; Canadian Light Source, Inc: Saskatoon, Canada, 2009; pp 156–157.